Propagation of Low-Mode Internal Waves through the Ocean

LUC RAINVILLE AND ROBERT PINKEL

Marine Physical Laboratory, Scripps Institution of Oceanography, La Jolla, California

(Manuscript received 26 November 2004, in final form 5 April 2005)

ABSTRACT

The baroclinic tides play a significant role in the energy budget of the abyssal ocean. Although the basic principles of generation and propagation are known, a clear understanding of these phenomena in the complex ocean environment is only now emerging. To advance this effort, a ray model is developed that quantifies the effects of spatially variable topography, stratification, and planetary vorticity on the horizontal propagation of internal gravity modes. The objective is to identify "baroclinic shoals" where wave energy is spatially concentrated and enhanced dissipation might be expected. The model is then extended to investigate the propagation of internal waves through a barotropic mesoscale current field. The refraction of tidally generated internal waves at the Hawaiian Ridge is examined using an ensemble of mesoscale background realizations derived from weekly Ocean Topography Experiment (TOPEX)/Poseidon altimetric measurements. The path of mode 1 is only slightly affected by typical currents, although its phase becomes increasingly random as the propagation distance from the source increases. The effect of the currents becomes more dramatic as mode number increases. For modes 3 and higher, wave phase can vary between realizations by $\pm\pi$ only a few wavelengths from the source. This phase variability reduces the magnitude of the baroclinic signal seen in altimetric data, creating a fictitious energy loss along the propagation path. In the TOPEX/Poseidon observations, the mode-1 M_2 internal tide does appear to lose significant energy as it propagates southwestward from the Hawaiian Ridge. The simulations suggest that phase modulation by mesoscale flows could be responsible for a large fraction of this apparent loss. In contrast, northeast-propagating internal tides encounter a less energetic mesoscale and should experience limited refraction. The apparent energy loss seen in the altimetric data on the north side of the ridge might indeed be real.

1. Introduction

Low-mode internal waves have been observed to propagate very long distances in the ocean. Mode-1 internal tides have been detected in satellite altimetry as far as 1000 km from generation sites along the Hawaiian Ridge (Ray and Mitchum 1996, 1997) and globally (Kantha and Tierney 1997). Using in situ sensors, a distinct tidal beam has been identified 450 km southwest of its generation on the Hawaiian Ridge (Rainville and Pinkel 2006). Energetic internal tidal waves have been seen 1000 km north of the Hawaiian Ridge (Dushaw et al. 1995; Chiswell 2002), and elevated baroclinic tidal energy has been detected in the Indian Ocean as far as 1700 km from the Mascarene Ridge, the probable wave generation site (Lozovatsky et al. 2003).

Low-mode internal tides rapidly fill the ocean interior in barotropically forced numerical models (Niwa and Hibiya 2001; Simmons et al. 2004). If these models are to be realistic, the mechanisms affecting wave propagation and dissipation must be understood. This problem has important implications for the geography of ocean mixing.

The ultimate fate of low-mode tidal waves remains an open question. St. Laurent and Garrett (2002) suggest a few possible mechanisms for the dissipation of the low-mode internal tide, including preferential dissipation in enhanced shear currents (such as the Antarctic Circumpolar Current) or propagation onto the continental shelves and resulting dissipation in shallow water (Nash et al. 2004). It is also possible that wave–wave interactions, such as the parametric subharmonic instability, might transfer energy from low to high vertical modes throughout the low-latitude (<28.9°) oceanic interior, eventually contributing to the background levels of open-ocean turbulence (Hibiya and Nagasawa 2004; MacKinnon and Winters 2005). The topographic scattering of internal waves (Müller and Xu 1992;

Corresponding author address: Luc Rainville, Woods Hole Oceanographic Institution, MS #21, Woods Hole, MA 02543.
E-mail: lrainville@whoi.edu

Johnston and Merrifield 2003) can, in principle, drain significant energy from the propagating tide.

Regions of slow group speed should experience an accumulation of wave energy relative to regions of high speed. Such sites ("baroclinic shoals") might be associated with enhanced mixing. Mapping the principal energy sources for the internal wave field [e.g., Egbert and Ray (2000) for barotropic tidal forcing and Alford (2003) for the wind input] is an essential first step toward understanding the geography of ocean mixing. The nonhomogeneity of the propagation environment must also be taken into account, however.

To interpret measurements of internal tide from satellite altimetry properly, it is also necessary to quantify propagation variability. Ocean Topography Experiment (TOPEX)/Poseidon (T/P) and *Jason-1* tracks repeat every 10 days. To extract the M_2 semidiurnal signal from other ocean processes, the existing 9-yr record must be harmonically fit to the M_2 frequency. This step isolates only the component of the signal that remains coherent with the astronomical tide. As internal waves propagate, variations in stratification and current can modify their phase and group speeds. In a long time series such as T/P, an increasing fraction of the M_2 signal will become incoherent with increasing distance from the source. To distinguish between true dissipation and loss of coherence, the propagation of internal tides in an inhomogeneous ocean must be understood.

This paper explores the processes that affect the propagation of the low-mode semidiurnal and near-inertial internal waves as they transit the oceans. In section 2, climatological density profiles are used to calculate the speed of propagation of mode 1 throughout the ocean. The nonuniformity of the ocean as a propagation medium is striking. Ray equations describing the horizontal propagation of internal wave modes are derived in section 3. Scattering processes are neglected. The case of nonuniform ocean depth and stability is first considered. The problem is then expanded in section 4 to include the effect of mesoscale currents. Examples relevant to the Hawaii Ocean Mixing Experiment (HOME) (Rudnick et al. 2003; Rainville and Pinkel 2006) and T/P observations are presented. It is found that mesoscale variability is sufficient to cause the M_2 internal tide generated at the Hawaiian Ridge to lose coherence with astronomical forcing as it propagates southward, generally consistent with the observed decay in the T/P signal. The tide propagating northward from the ridge should experience less mesoscale variability. The T/P finding of a rapid apparent northward decay thus suggests that the mode-1 tide is in fact losing energy, or at least deviating from the satellite ground track.

2. Group and phase velocities of internal wave modes

Formulated in terms of the wave vertical velocity w, the equation governing low-frequency ($\omega \ll N$) baroclinic modal propagation, with $w = \tilde{w}(x, y)\hat{w}(z)\exp(-i\omega t)$, is

$$\left(\frac{1}{N^2}\frac{d^2}{dz^2}\right)\hat{w} + \left[\frac{(\partial_{xx} + \partial_{yy})\tilde{w}}{(-\omega^2 + f^2)\tilde{w}}\right]\hat{w} = 0. \quad (1)$$

Here f is the Coriolis frequency and N is the buoyancy frequency. With $\hat{w} = 0$ at the sea surface ($z = 0$) and seafloor ($z = -D$), Eq. (1) is an eigenvalue problem. The left-hand term is a function of z only, operating on the eigenvector $\hat{w}(z)$, with

$$\left[\frac{(\partial_{xx} + \partial_{yy})\tilde{w}}{(-\omega^2 + f^2)\tilde{w}}\right] \equiv \frac{1}{c_e^2}. \quad (2)$$

A given buoyancy frequency profile defines a set of modes and their corresponding eigenvalues. By rearranging Eq. (2), the Helmholtz equation for internal wave modes is obtained:

$$\left(\partial_{xx} + \partial_{yy} + \frac{\omega^2}{c_e^2} - \frac{f^2}{c_e^2}\right)\tilde{w} = 0. \quad (3)$$

Free wave solutions of the form $\tilde{w}(x, y) = A\exp[i(k_x x + k_y y)]$ exist, provided that

$$\omega^2 - f^2 = (k_x^2 + k_y^2)c_e^2. \quad (4)$$

For reference, the horizontal wavelength $[k_H^{-1} = (k_x^2 + k_y^2)^{-1/2}]$ of the M_2 internal tide in deep water near Hawaii is approximately 150 km for mode 1, 80 km for mode 2, and 50 km for mode 3. Given the dispersion relation, the group speed along the direction of propagation is

$$c_G \equiv \frac{\partial\omega}{\partial k_H} = \frac{(\omega^2 - f^2)^{1/2}}{\omega}c_e. \quad (5)$$

In a similar way, the phase speed for each mode is

$$c_P \equiv \frac{\omega}{k_H} = \frac{\omega}{(\omega^2 - f^2)^{1/2}}c_e, \quad (6)$$

such that $c_G c_P = c_e^2$.

To quantify global propagation conditions, buoyancy frequency profiles have been calculated over the world oceans using the climatological temperature and salinity obtained from S. Levitus's *World Ocean Atlas 2001* (Stephens et al. 2002; Boyer et al. 2002). With knowl-

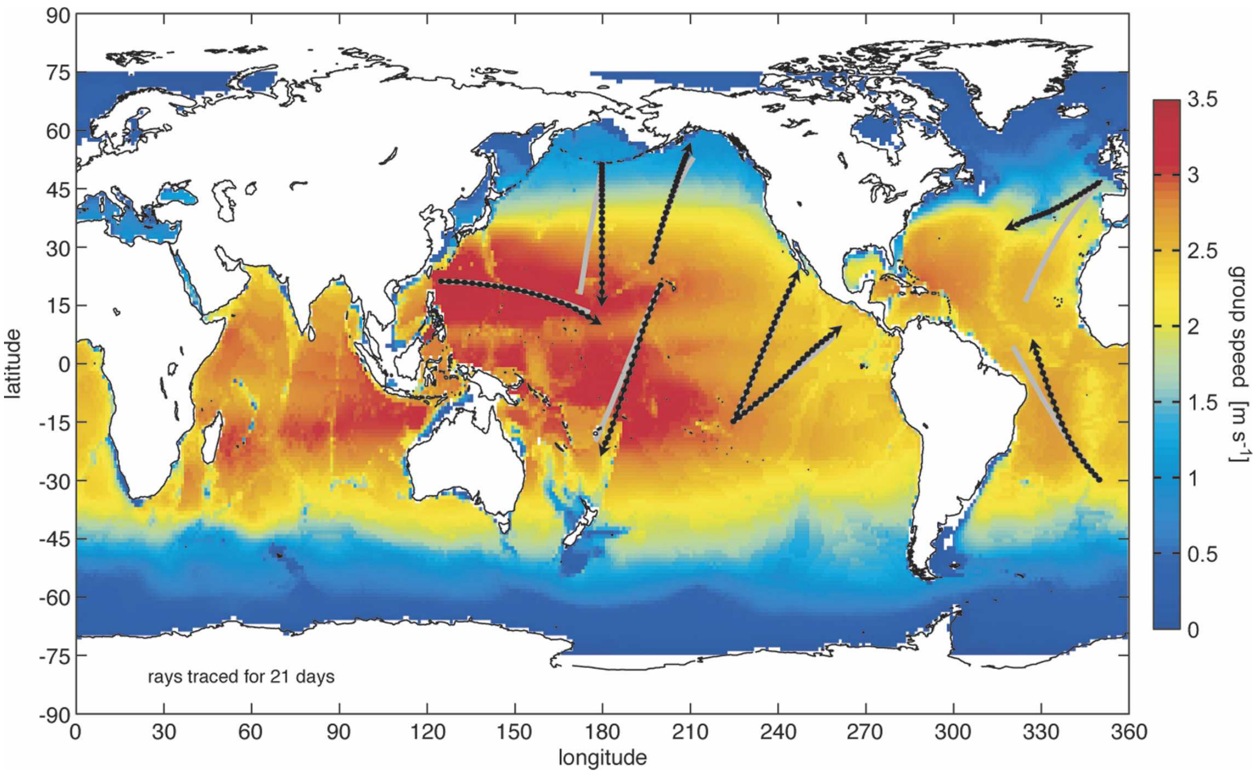

FIG. 1. Group speed of mode-1 M_2 internal tide over the entire world. Representative rays emanating from known generation sites are also plotted in black. Circles indicate the daily position of the group over a 3-week period. Rays calculated considering only the latitudinal dependence (neglecting ocean depth and buoyancy variability) are plotted in gray.

edge of the stratification and seafloor topography, Eq. (1) is then solved at each grid point (1° in latitude and longitude; thus 180 × 360 points), leading to global maps of c_e. The associated group and phase speeds of a mode-1 M_2 internal tide, obtained from Eqs. (5) and (6), are shown in Figs. 1 and 2. Note that the group speed vanishes at the turning latitude (where the wave is purely inertial; 75° for M_2), whereas the phase speed approaches infinity.

Buoyancy frequency, latitude, and water depth jointly affect the group and phase speeds. The group and phase speeds are both reduced significantly in shallower areas. For example, over the Mid-Atlantic Ridge, from 25° to 5°S, the group speed of a mode-1 packet is about 2.1 m s^{-1}. The same wave propagates 30% faster at over 2.7 m s^{-1} in the Brazil Basin. Similarly, the East Pacific Rise, the Izu–Ogasawara Ridge, the Somali Basin, and so on, have clear signatures on the speed maps.

The most dramatic shoal is at high latitude, because of both $f(y)$ and $N(y)$. The decay of group speed and growth of phase speed with latitude, established by the latitudinal dependence of f in Eqs. (5) and (6), is emphasized by forming zonal averages of the mode-1 speed (Fig. 3). The dashed lines give the comparable group and phase speeds for an ocean of constant depth and buoyancy frequency.

Even in the zonal averages, the effect of variation in stratification is seen. The sharp decrease in M_2 group and phase speeds poleward of 30°–35° reflects the difference in buoyancy frequency in the subtropical and subpolar gyres (Fig. 4). In the subtropical Pacific Ocean (e.g., 15°N, 180°), the water column is highly stratified. The buoyancy frequency typically peaks at a value near 8 cycles per hour (cph) at depths of 150 m. In contrast, a representative buoyancy frequency profile in the subpolar gyre (e.g., 50°N, 180°) has a maximum of 4 cph at 100 m. The reduction in upper-ocean stability results in a smaller c_e and a corresponding decrease in both the phase and group speeds [Eqs. (5) and (6)]. Also, the western Pacific is in general deeper and more stratified than the eastern side, resulting in a large-scale propagation speed gradient.

The net effect of the buoyancy frequency, depth, and latitude variations is to create the global pattern seen in Fig. 1: the group speed is large and relatively homogeneous within 30°–35° of the equator, dropping sharply poleward of the Tropics.

In addition to the tides, a storm (or hurricane) mov-

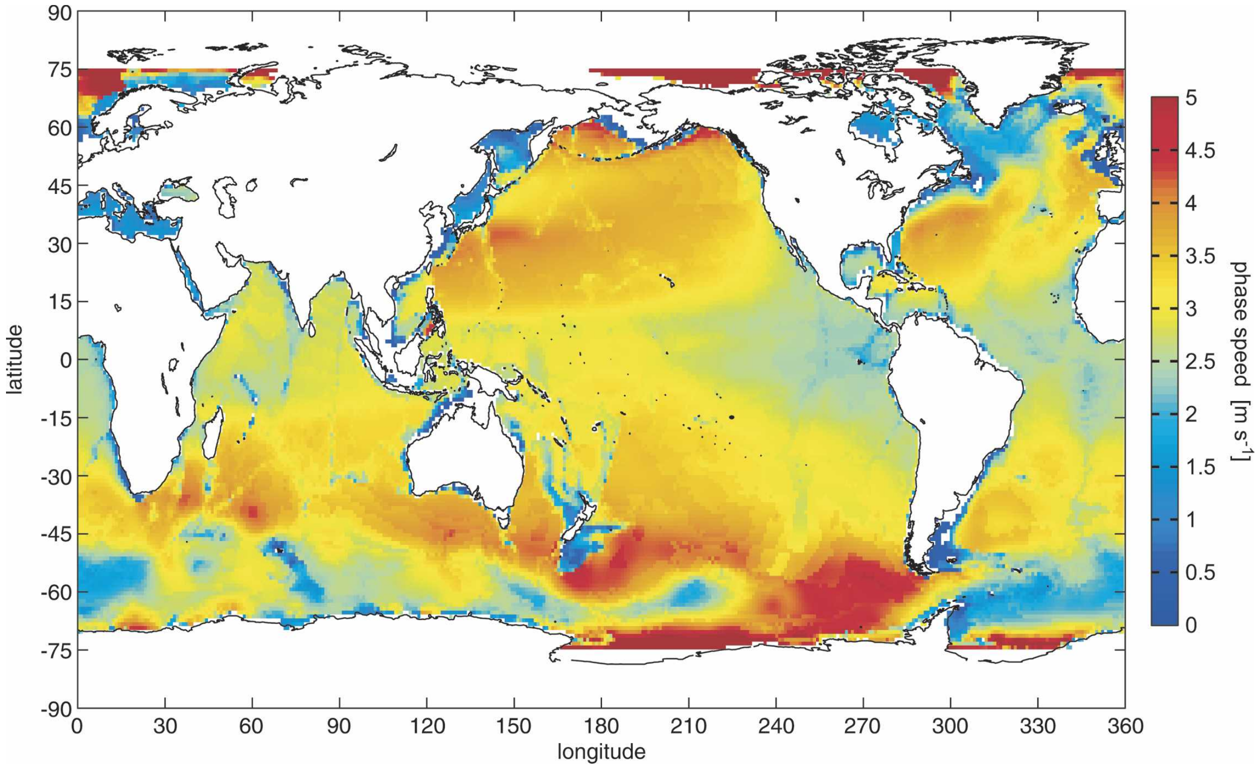

FIG. 2. Global map of the phase speed of mode-1 M_2 internal tide.

ing across the ocean generates waves spanning a wide range of vertical modes (Gill 1982). Alford (2001, 2003) computes the energy input from the wind to inertial mixed layer motions using global National Centers for Environmental Prediction–National Center for Atmospheric Research reanalysis surface winds. When comparing with data, he finds the near-inertial internal wave energy flux computed at several moorings to be generally consistent with equatorward propagation of low-mode near-inertial internal waves. To extend his study, we show (Fig. 5) the group speed for a mode-1 internal wave with a period of 17 h, corresponding to a

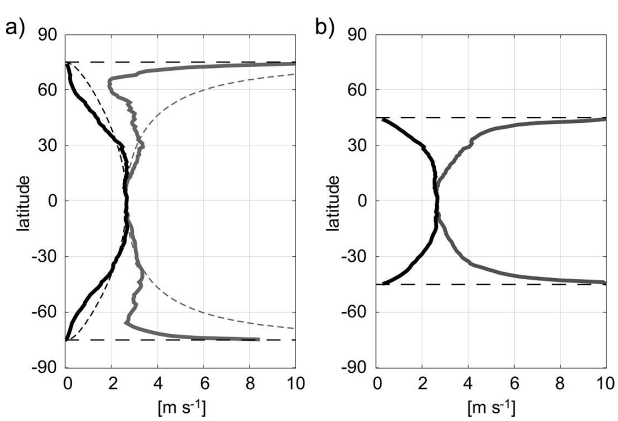

FIG. 3. Zonal average of the group (black) and phase (gray) speeds (a) for an M_2 and (b) for a 17-h-period mode-1 internal wave. The dashed lines in (a) only take the latitude dependence into account. Long-dashed lines are the turning latitudes.

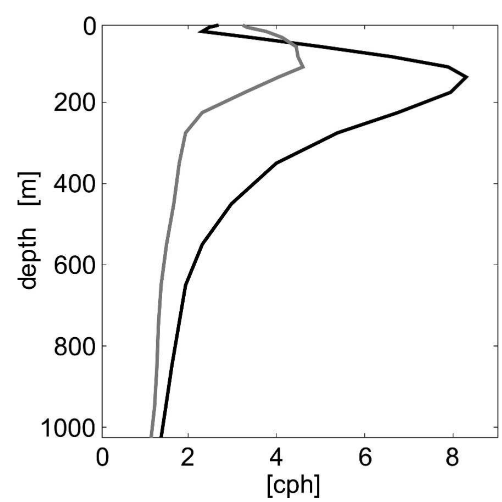

FIG. 4. Buoyancy frequency profiles in the upper 1000 m in the North Pacific subtropical (black line, at 15°N, 180°) and subpolar (gray line, at 50°N, 180°) gyres. Stratification is stronger in the subtropical gyre.

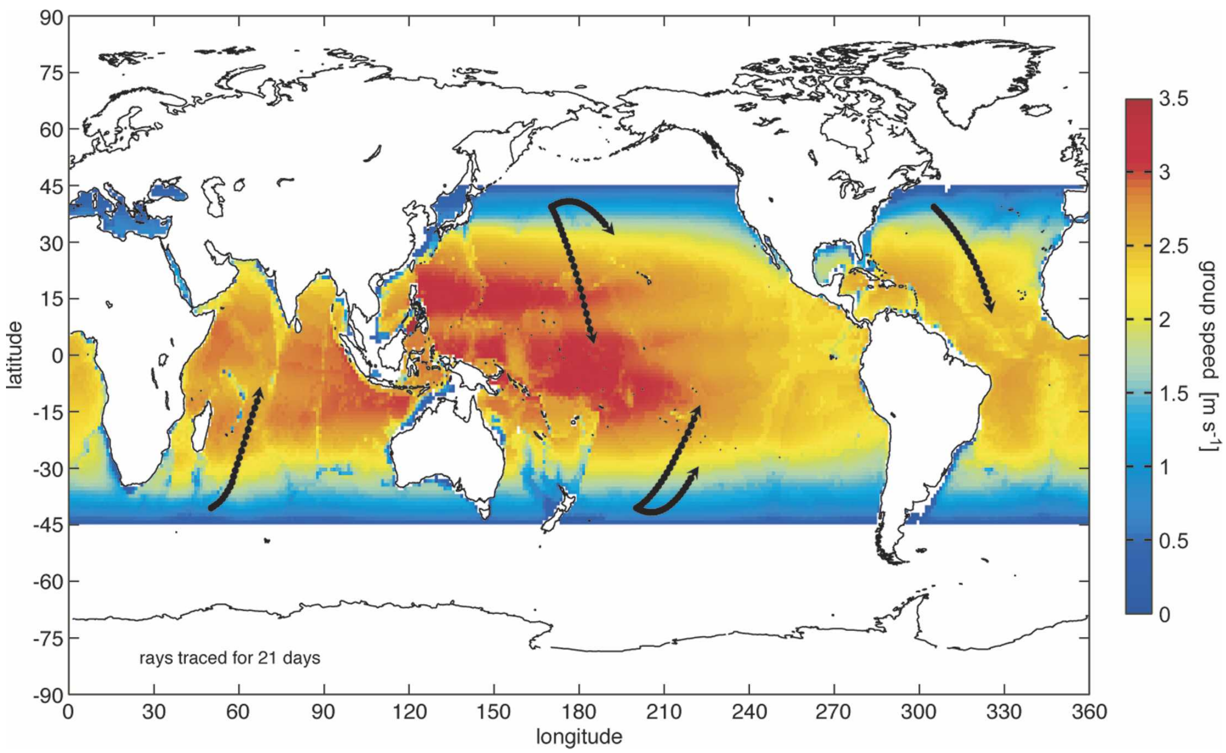

FIG. 5. Global map of the group speed of mode-1 internal wave whose frequency corresponds to a turning latitude of 45°. Several rays emanating from regions of frequent storms are also plotted. Circles indicate the daily position of the group over a 3-week period.

turning latitude of 45°. Such a wave is purely inertial at a latitude just poleward of most storm tracks (Alford 2001). The global pattern is similar to the M_2 internal tide propagation pattern, although the relatively low turning latitude greatly reduces the relative effects of buoyancy and depth variability. The zonal average (Fig. 3b) mostly reflects the latitudinal dependence.

3. Ray equations: Propagation through a nonhomogeneous medium

a. Latitude, buoyancy, and depth variability

In this section, the ray equations for the horizontal propagation of an internal wave mode through a rotating ocean of spatially varying buoyancy and depth are derived. Here, c_e in Eq. (2) is a function of position only. This problem is similar to that of acoustic propagation in a range-dependent sound speed channel. The solution derived here is an extension of Colosi (2006) and Lighthill (2002).

The Helmholtz equation for internal wave modes, Eq. (3), is solved in the so-called geometric limit, where it is assumed that the horizontal dependence of the wave $[\tilde{w}(x, y)]$ is a varying sinusoid:

$$\tilde{w} = A(x, y) \exp[i\omega\phi(x, y)], \tag{7}$$

where A is a slowly varying function of x and y [or longitude and latitude, with $dx \sim d(\mathrm{lon}) \times \cos(\mathrm{lat})$]. Substituting Eq. (7) into Eq. (3) and retaining only the real part leads to

$$[\partial_{xx}A - A\omega^2(\partial_x\phi)^2] + [\partial_{yy}A - A\omega^2(\partial_y\phi)^2] + \frac{A\omega^2}{c_e^2} - \frac{Af^2}{c_e^2} = 0. \tag{8}$$

Because A varies only slowly in x and y, the terms multiplied by ω^2 are larger than those involving $\partial_{x_i x_i}A$. In the limit $\nabla_H^2 A/\omega^2 \ll 1$,

$$(\partial_x\phi)^2 + (\partial_y\phi)^2 - \frac{1}{c_P^2} = 0, \tag{9}$$

where the definition of the phase speed [Eq. (6)] has been used. As a means to obtain ray solutions, a Hamiltonian function $H(p_x, p_y, x, y)$ can be defined

$$H \equiv p_x^2 + p_y^2 - \frac{1}{c_P^2}, \tag{10}$$

where $(p_x, p_y) \equiv \nabla\phi$. The goal here is to find a curve in (x, y) space parameterized by a variable λ [i.e., $x(\lambda)$ and

$y(\lambda)]$ such that $H = 0$ along that curve. In mathematic terms, this statement is expressed as

$$\frac{dH}{d\lambda} = \frac{\partial H}{\partial p_i}\frac{dp_i}{d\lambda} + \frac{\partial H}{\partial x_i}\frac{dx_i}{d\lambda} = 0, \tag{11}$$

where summation over repeating indices is implied. Here $p_i = (p_x, p_y)$ and $x_i = (x, y)$. The condition that $H = 0$ along the curve is equivalent to requiring that

$$\frac{dp_i}{d\lambda} = -\frac{\partial H}{\partial x_i} \quad \text{and} \tag{12}$$

$$\frac{dx_i}{d\lambda} = +\frac{\partial H}{\partial p_i} \tag{13}$$

are satisfied. Equations (12) and (13) are called the Hamilton's equations.

Ray solutions are found by solving Eqs. (12) and (13) using a Hamiltonian appropriate for internal-wave modal propagation. Using Eq. (10) we get

$$\frac{dx}{d\lambda} = \frac{\partial H}{\partial p_x} = 2p_x \quad \text{and} \tag{14}$$

$$\frac{dy}{d\lambda} = \frac{\partial H}{\partial p_y} = 2p_y. \tag{15}$$

The ray propagation direction is therefore

$$\frac{dy}{dx} = \frac{p_y}{p_x} \equiv \tan\theta, \tag{16}$$

where θ is the angle of propagation measured clockwise from east. Setting $H = 0$ in Eq. (10) and using Eq. (16), we find

$$p_x = \frac{\cos\theta}{c_P}. \tag{17}$$

The variation of p_y along the ray is given by

$$\begin{aligned}\frac{dp_y}{dx} = \frac{dp_y}{d\lambda}\frac{d\lambda}{dx} &= -\frac{\partial H}{\partial y}\frac{d\lambda}{dx}\\ &= -\frac{1}{c_P^3}\frac{1}{p_x}\frac{\partial c_P}{\partial y}\\ &= -\frac{1}{c_e^2\omega^2 p_x}\left[(p_x^2 + p_y^2)c_e\omega^2\frac{\partial c_e}{\partial y} + f\frac{\partial f}{\partial y}\right].\end{aligned} \tag{18}$$

As an alternative, a pair of equations eliminating p_y and describing the variation of p_x with respect to y can be derived to replace Eqs. (17) and (18). Given an initial position and the direction of propagation, the initial p_x and p_y are obtained from Eqs. (16) and (17). The propagation path of the ray is then found by solving Eqs. (16)–(18) numerically. The alternate formulation in terms of dp_y/dy is useful when $dx \to 0$ ($\theta \sim \pm\pi/2$).

Equation (18) provides insight on the propagation of internal waves through a nonhomogeneous ocean. For free waves, $\phi = \omega^{-1}(k_x x + k_y y)$; thus p_x and p_y correspond to the local wavenumbers (normalized by ω). Equation (18) shows that the wavenumber decreases in the direction of positive phase speed gradient. Waves therefore tend to be refracted away from regions of high phase speed. Note that the group velocity, $\mathbf{c}_G = (\partial\omega/\partial k_x, \partial\omega/\partial k_y)$, estimated from Eq. (4), is directed along the propagation path (i.e., $c_{G_y}/c_{G_x} = dy/dx = k_y/k_x$). Because only horizontal propagation is considered here (the problem is formulated in terms of modes), the phase velocity

$$\mathbf{c}_P = \left[\frac{k_x}{(k_x^2 + k_y^2)^{1/2}}, \frac{k_y}{(k_x^2 + k_y^2)^{1/2}}\right]c_P \tag{19}$$

is in the same direction as the group velocity, although their magnitudes (speeds) are different.

Looking at the effects of f and c_e separately [Eq. (18)], one sees that waves are always refracted toward the equator because $-f\partial f/\partial y$ is negative in the Northern Hemisphere (decreasing northward wavenumber) and positive in the Southern Hemisphere (increasing northward wavenumber). In a similar way, a positive gradient of c_e along a given direction will decrease the wavenumber in that direction.

For example, a set of rays for M_2 internal waves with a uniform $c_e(x, y) = 3\ \mathrm{m\,s^{-1}}$ (roughly the averaged mode-1 speed at the equator) is plotted in Fig. 6a. Mode-1 groups are started at 0°, 10°E for initial propagation angles of 10°, 20°, 40°, 60°, and 80° with respect to the x axis. The rays are plotted for a propagation time of 140 days. The phase and group velocities as functions of latitude are plotted in Fig. 6b. The direction of the rays is controlled by refraction toward regions of small phase speed.

Figure 6a is reminiscent of the ray pattern of sound propagation through a vertical–horizontal oceanic waveguide (e.g., Jensen et al. 2000), with a typical depth profile of sound speed similar to the meridional profile of baroclinic phase speed here (Fig. 3). However, because the Helmholtz equation for sound is

$$\left(\partial_{xx} + \partial_{yy} + \frac{\omega^2}{c^2}\right)\tilde{\Psi} = 0, \tag{20}$$

instead of Eq. (3) for internal waves, the group and phase speeds for a sound wave are identical. In acoustics, a sound wave launched at an initially high initial angle relative to the horizontal spends fractionally more time in regions of high group speed than low. It arrives at a given range earlier than a wave launched at a lower angle. The reverse situation occurs for internal

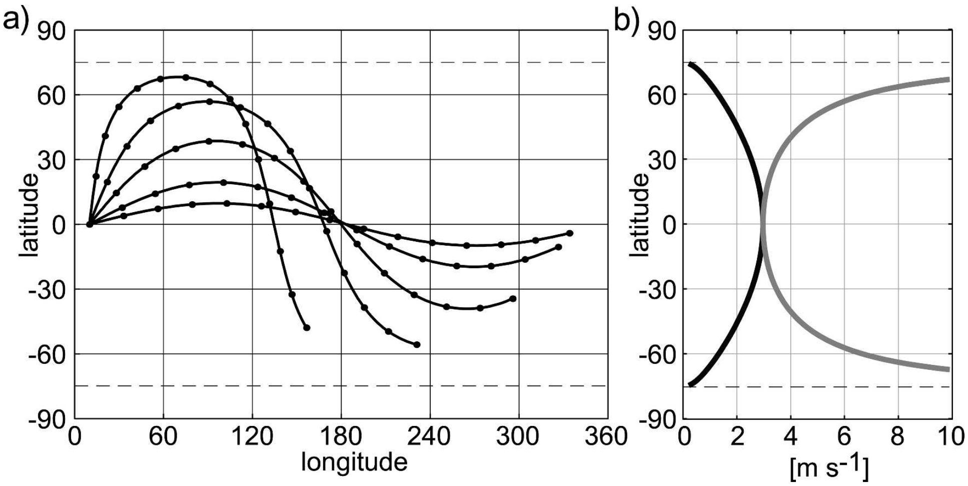

FIG. 6. (a) Rays for an M_2 mode-1 baroclinic wave, considering only the latitudinal dependence of c_P and c_G. All rays are started at 0°, 10°E but for initial propagation angles of 10°, 20°, 40°, 60°, and 80° with respect to the x axis. Positions every 10 days are indicated by circles. (b) Group (black) and phase (gray) speed as functions of latitude. The turning latitude is indicated by the dashed lines.

wave modes because the group speed near the turning latitude is much smaller than near the equator (Fig. 6a).

Using the nonuniform c_e computed in the previous section, several rays of mode-1 internal waves emanating from suspected generation regions are plotted in Figs. 1 and 5. For the M_2 waves (Fig. 1), source regions are chosen to be sites of strong generation as seen in numerical models (e.g., Simmons et al. 2004). The initial directions of propagation are chosen more or less arbitrarily perpendicular to topography. Rays with the same initial conditions but sensitive only to rotational effects (i.e., c_e = constant) are plotted in gray. Circles indicate the daily position of the group. Generation regions for wind-generated waves (Fig. 5) are chosen from the regions of strong energy input for the winds (Alford 2001). Note how near-inertial waves traveling poleward and being refracted toward the equator propagate only short distances, because the group speed is greatly reduced near the turning latitude. In converse, the waves propagating equatorward can travel several thousand kilometers in 3 weeks.

The combined effects of latitude, bathymetry, and stratification are illustrated in Fig. 7, which presents mode-1 M_2 rays propagating through the Brazil Basin. Rays are started at the Mid-Atlantic Ridge with initial propagation angles of 100°, 120°, 140°, 160°, and 185° with respect to the east. Propagation paths obtained from the calculated $c_e(x, y)$ (black lines; c_P depends on latitude, stratification, and depth) and those computed taking c_e = constant (gray lines; c_P is a function of latitude only) are presented for comparison. Refraction away from the regions of high c_e (indicated by the color map) is evident.

The mode-2 $c_e(x, y)$ is similar to the mode-1 $c_e(x, y)$ but reduced by approximately a factor of 2.[1] The normalized spatial variation $c_e^{-1}(\partial c_e/\partial x_i)$ is identical for the different modes, implying that the propagation paths of higher modes are almost indistinguishable from the path of mode 1 [Eq. (18)].

b. Latitude, buoyancy, depth, and barotropic current variability

The goal of this section is to generalize the preceding derivation to consider barotropic mesoscale current $\{\mathbf{U} = [U(x, y), V(x, y)]\}$ variability, as well as that of buoyancy and ocean depth. The discussion is again centered on the linearized internal wave equation, which, in the presence of advection (see appendix A), takes the form

$$[(\partial_t + \mathbf{U}\cdot\boldsymbol{\nabla})^2\nabla^2 + f^2\partial_{zz} + N^2(\partial_{xx}+\partial_{yy})]w = 0. \quad (21)$$

Phillips (1977) derived a more general result (the Taylor–Goldstein equation) for the nonrotational case, considering a depth-dependent background current. For internal tides and near-inertial waves propagating through a barotropic current, the resulting equation for the vertical dependence of the modes is of the same form as in the current-free case, although the eigenvalues become dependent on the direction and speed of both the current and the wave (appendix B).

There have been several studies (Müller 1976; Olbers 1981; Kunze 1985; Young and Ben Jelloul 1997;

[1] In constant stratification, the eigenvalues are $c_e = NH(n\pi)^{-1}$, where n is the mode number (Gill 1982).

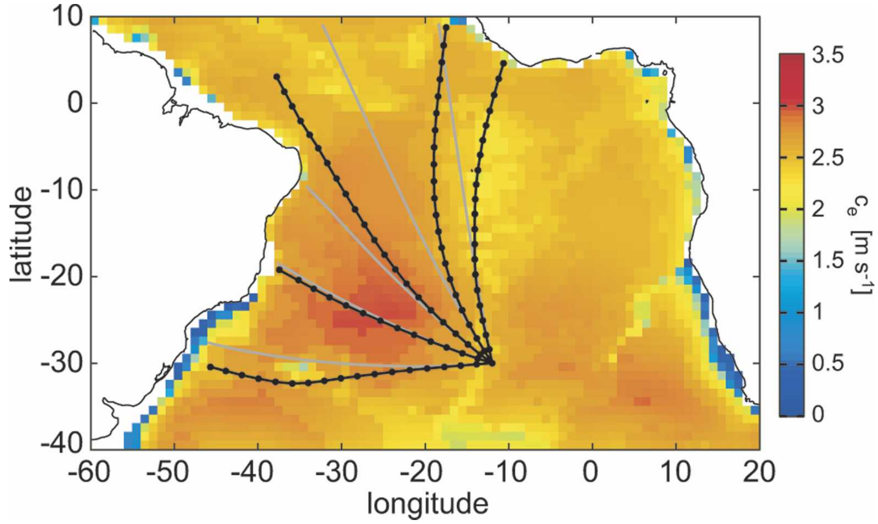

FIG. 7. Rays for an M_2 mode-1 wave generated at the Mid-Atlantic Ridge and propagating through the Brazil Basin. Rays are started at 30°S, 12°W with initial propagation angles of 100°, 120°, 140°, 160°, and 185° with respect to the east. Daily positions are indicated by circles. Propagation paths considering only the latitudinal effect are plotted in gray. The color map indicates c_e.

Miropol'sky 2001; Jones 2001) of the interaction of geostrophic currents on low-frequency internal waves. Using ray tracing, Kunze (1985) has shown the refractive effect of geostrophic shear on free near-inertial waves. Thorpe (1978) has similarly used the formal expression derived in Phillips (1977) to compute the internal-wave function in the case of constant $N(z)$ and shear (d_zU), and in the case in which N and d_zU are confined to a narrow transition layer.

In this work, only a depth-independent current is considered. This restriction is not overly limiting when considering how the first few modes interact with a mesoscale flow with large spatial scales. The vorticity of the mesoscale flow considered in this study is small relative to the planetary vorticity. Vertical shear is also small. Therefore, the depth dependence of the relevant term in the Taylor–Goldstein equation, $[c - U(z)]^{-2}$ (Munk 1981), can be neglected for the first few modes, and it is not necessary to take into account the vertical shear of the background flow in the calculation of the vertical modes, as in Peters (1983). The formulation in terms of modes emphasizes the present focus on horizontal propagation, with the objective of developing physical intuition and advancing data interpretation.

In the presence of barotropic currents, a new linear Hamiltonian function is obtained (see appendix B):

$$H \equiv (c_e^2 - U^2)p_x^2 + (c_e^2 - V^2)p_y^2 + 2Up_x + 2Vp_y - 2UVp_xp_y - 1 + \frac{f^2}{\omega^2}, \tag{22}$$

where $\nabla\phi = (p_x, p_y)$. The last two terms can be written as $c_e^2c_P^{-2}$, but, to avoid mixing the different wave speeds, we retain the formulation in terms of c_e. As before, rays are defined as curves along which $H = 0$, that is, along the solution of Eqs. (12) and (13). The solution is

$$\frac{dx}{d\lambda} = \frac{\partial H}{\partial p_x} = 2(c_e^2 - U^2)p_x + 2U - 2UVp_y \quad \text{and} \tag{23}$$

$$\frac{dy}{d\lambda} = \frac{\partial H}{\partial p_y} = 2(c_e^2 - V^2)p_y + 2V - 2UVp_x. \tag{24}$$

The angle of the propagation of the ray is therefore

$$\frac{dy}{dx} = \frac{2(c_e^2 - V^2)p_y + 2V - 2UVp_x}{2(c_e^2 - U^2)p_x + 2U - 2UVp_y} \equiv \tan\theta. \tag{25}$$

From Eq. (22), the equation $H = 0$ is quadratic in p_x. Therefore,

$$\begin{aligned} p_x &= \frac{-b \pm (b^2 - 4ac)^{1/2}}{2a}, \quad \text{where} \\ a &= c_e^2 - U^2, \\ b &= 2U(1 - Vp_y), \quad \text{and} \\ c &= (c_e^2 - V^2)p_y^2 + 2Vp_y - 1 + \frac{f^2}{\omega^2}. \end{aligned} \tag{26}$$

The sign of the square root is chosen so that the sign of p_x agrees with the angle of propagation. The equation describing the variation of p_y as a function of x is found as in Eq. (18):

$$\frac{dp_y}{dx} = -\frac{\partial H}{\partial y}\frac{d\lambda}{dx}, \tag{27}$$

where $d\lambda/dx$ is given by Eq. (23) and

$$\frac{\partial H}{\partial y} = 2c_e(p_x^2 + p_y^2)\frac{\partial c_e}{\partial y} - 2(Up_x^2 - p_x + Vp_xp_y)\frac{\partial U}{\partial y} - 2(Vp_y^2 - p_y + Up_xp_y)\frac{\partial V}{\partial y} + \frac{2f}{\omega^2}\frac{\partial f}{\partial y}. \tag{28}$$

As in section 3a, Eqs. (26) and (27) can be replaced by equivalent expressions for p_y and dp_x/dy when $dx \to 0$. Given an initial position and propagation angle, the propagation path is found as outlined in the last section but using the generalized equations derived above. The initial p_x and p_y can be found from Eqs. (25) and (26). Then, for each step, Eq. (27) specifies the change in p_y. Equation (26) is then used to find the corresponding new value of p_x, and the new propagation angle is given by Eq. (25).

Currents affect the dispersion relation and modify the group velocity. As in section 2, the dispersion relation is obtained from the Helmholtz equation by assuming that the wave has a local expression of the form $w = A\exp[i(k_xx + k_yy - \omega t)]$. Substituting in Eq. (22) and retaining the real part only, we obtain

$$-k_x^2(c_e^2 - U^2) - k_y^2(c_e^2 - V^2) - 2\omega Uk_x - 2\omega Vk_y + 2UVk_xk_y + \omega^2 - f^2 = 0. \tag{29}$$

By differentiating with respect to k_x and rearranging, we obtain

$$c_{G_x} \equiv \frac{\partial\omega}{\partial k_x} = \frac{k_x(c_e^2 - U^2) + \omega U - UVk_y}{\omega - Uk_x - Vk_y}. \tag{30}$$

Differentiation with respect to k_y similarly leads to

$$c_{G_y} \equiv \frac{\partial\omega}{\partial k_y} = \frac{k_y(c_e^2 - V^2) + \omega V - UVk_x}{\omega - Uk_x - Vk_y}. \tag{31}$$

Equations (26) and (27) enable the determination of p_x and p_y along the ray path. For slowly varying amplitude and phase, we see that locally $\tilde{w}(x, y) = A\exp(i\omega\phi) = A\exp[i(k_xx + k_yy)]$, implying that $k_x \simeq \omega p_x$ and $k_y \simeq \omega p_y$. The group velocity $\mathbf{c}_G = (\partial\omega/\partial k_x, \partial\omega/\partial k_y)$ along the propagation path of a mode in the presence of currents is therefore found from Eqs. (30) and (31), using the properties of the waves found during the integration of Eqs. (25)–(27). The group velocity is directed along the propagation path but is no longer parallel to the phase velocity (i.e., $c_{G_y}/c_{G_x} = dy/dx \neq k_y/k_x$). The travel time for energy is simply the integral of the reciprocal of the group velocity [obtained from Eqs. (30) and (31)] along the propagation path.

4. Propagation through the mesoscale velocity field near Hawaii

a. Mesoscale velocities from altimetric data

The mesoscale velocity field near Hawaii can be estimated from the sea surface height maps produced by the Archiving, Validation, and Interpretation of Satellite Oceanographic Data (Aviso)/Altimetry project. The Aviso maps provide weekly sea surface height anomalies relative to a 7-yr mean (January 1993–January 1999). Height anomalies are obtained using the objective mapping method detailed in Ducet et al. (2000), merging measurements recorded from the T/P and European Remote Sensing Satellite altimeters.[2] Geostrophic currents are obtained from the surface topography, $\zeta(x, y)$, using (Gill 1982):

$$U_{\text{sfc}}(x, y) = \frac{-g}{f}\frac{\partial\zeta}{\partial y} \quad \text{and} \tag{32}$$

$$V_{\text{sfc}}(x, y) = \frac{+g}{f}\frac{\partial\zeta}{\partial x}. \tag{33}$$

In the Aviso maps, the temporal correlation scale at midlatitude is set to 15 days (decreasing to 10 days equatorward of 10°) and the space correlation scales, taken to represent the dominant length scale of the eddy field, are (Ducet et al. 2000)

$$L = 50 + 250\left(\frac{900}{\text{Lat}^2 + 900}\right)\text{ km}, \tag{34}$$

where Lat stands for latitude (°). At Hawaii, this corresponds to about 220 km. Because mesoscale space and time scales are (marginally) larger than wavelengths and propagation times, we are (marginally) justified in applying the time-independent Wentzel–Kramers–Brillouin (WKB) approach.

The large correlation scale of the Aviso product smooths over the submesoscale stucture present in the ocean. In particular, the North Pacific subtropical front, extending across the entire basin at about 30°N, sometimes has a width as small as ~10 km with speeds of 0.1 m s^{-1} (Kunze and Sanford 1984; Ferrari and Rudnick 2000). In using the Aviso maps, this model ignores the submesoscale structure of the ocean and concentrates on the effect of the large mesoscale eddies.

[2] The altimeter products were produced by the Segment Sol Multimissions d'Altimétrie, d'Orbitographie et de Localisation Précise/Data Unification and Altimeter Combination System (Ssalto/Duacs) as part of the Environment and Climate European Union ENACT project (EVK2-CT2001–00117) and distributed by Aviso, with support from the Centre National d'Études Spatiales (CNES).

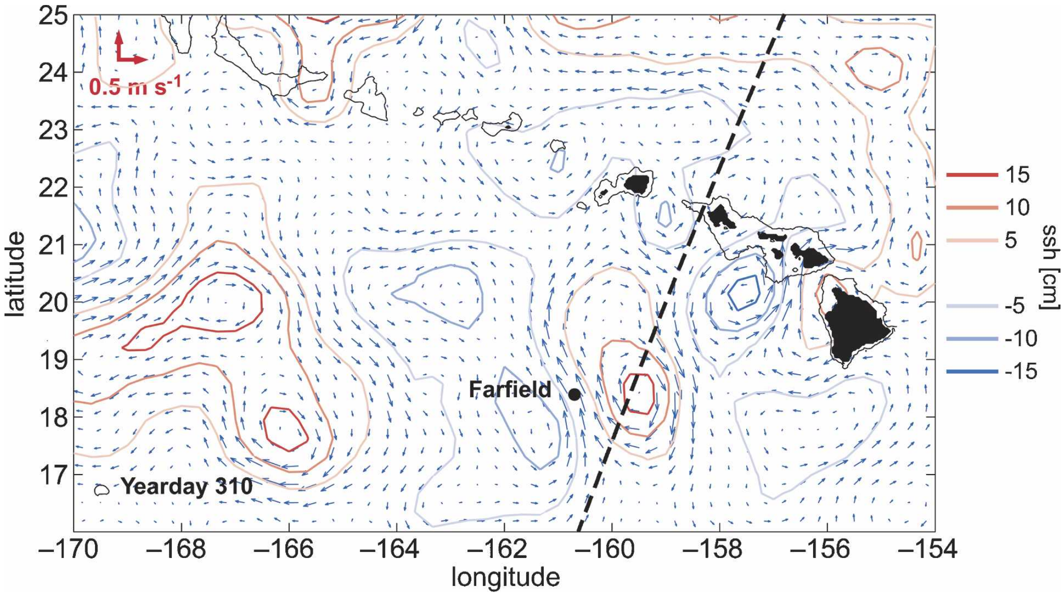

FIG. 8. Sea surface height and surface geostrophic currents near Hawaii during the last week of the HOME Farfield program (yearday 310). Geostrophic velocities estimated from the surface height are plotted as vectors. The T/P track 112 is indicated by the dashed line.

Sea surface elevation anomalies during the last week of the HOME Farfield Research Platform (R/P) *Floating Instrument Platform* (*FLIP*) deployment (Rainville and Pinkel 2006) are presented in Fig. 8, along with the inferred currents from Eqs. (32) and (33). A direct comparison of geostrophic velocity derived from the Aviso altimetric data and in situ observations from the R/P *FLIP* at the HOME Farfield site (18.39°N, 160.70°W), low-pass filtered to retain only subinertial frequencies, is shown in Fig. 9. Aviso velocities reproduce the magnitude and direction of the near-surface subinertial currents, validating the Aviso analysis as a tool to obtain the mesoscale eddy field accurately.

Equations (32) and (33) give only the geostrophic surface currents ($\mathbf{U}_{\mathrm{sfc}}$). The model considers the barotropic component of the current field, which is generally smaller than the surface current. In fact, subinertial velocities measured by *FLIP* at the HOME Farfield site are observed to decrease slowly with depth in the upper 900 m. Ad hoc comparisons between our simple propagation model and along-track T/P data, filtered to detect mode-1 waves (presented in section 4c), suggest that barotropic subinertial currents are best represented by approximately ~½ the magnitude of the geostrophic current calculated from sea surface elevations. This suggests small vertical shear for the mesoscale flow. The fraction of ½ is perhaps larger than would normally be expected (Wunsch 1997). The eddies south of Hawaii are primarily generated by the topographic interaction of large-scale currents with the island of Hawaii rather than being wind-driven, however, possibly leading to a different vertical structure. In addition, the vertical vorticity associated with the mesoscale field resolved by Aviso is very small: the magnitude of the relative vorticity calculated from surface currents never exceeds 20% of the Coriolis frequency. No trapping or amplification is expected (Kunze 1985). Neglecting the interaction terms involving the mean flow shear [terms of the form $(\mathbf{u} \cdot \boldsymbol{\nabla})\mathbf{U}$ in the equation of motion in appendix A] when considering interactions of low modes with large-scale geostrophic flow derived from altimetry therefore seems justified.

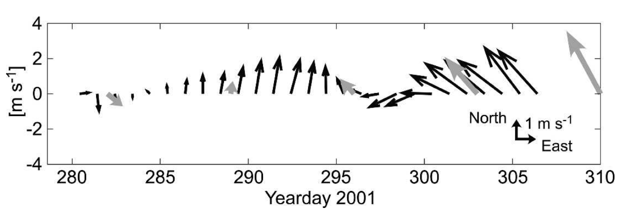

FIG. 9. Comparison between upper-ocean subinertial velocities ($\omega < 1/40$ cph) estimated using a Doppler sonar deployed from the R/P *FLIP* (black vectors) and geostrophic velocities derived from satellite sea surface height estimates (gray vectors). The in situ data are averaged between 80 and 150 m.

b. *Internal wave propagation to the HOME Farfield site*

To illustrate the effect of mesoscale currents on internal waves, we consider the propagation of baroclinic

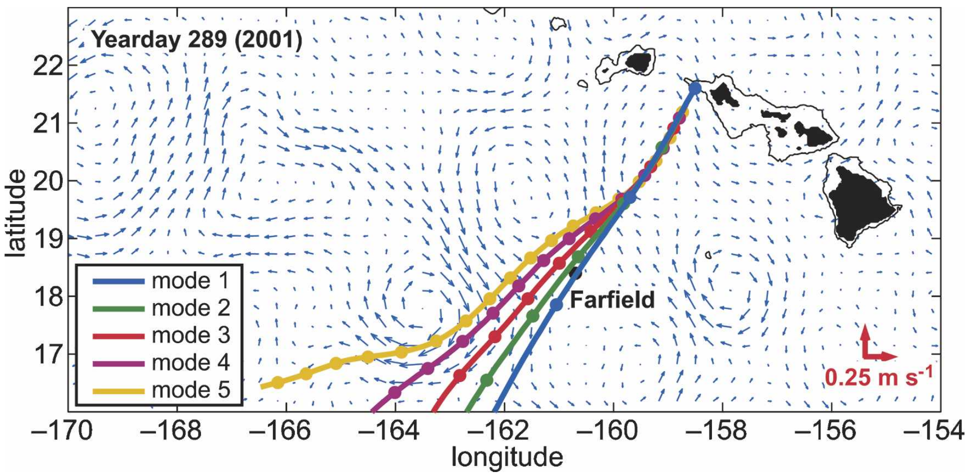

FIG. 10. Propagation paths of modes 1–5 generated in the Kauai Channel and traveling though the mesoscale eddy field seen during the week of 16 Oct 2001. Currents are derived from sea surface height measured by satellite altimeters (adjusted by a factor of ½). Daily positions of the modes are indicated by the solid circles.

modes from the Kauai Channel west of Oahu to the HOME Farfield site. Figure 10 shows the paths of modes 1–5 propagating through the mesoscale flow during the second week of the Farfield program. Rays are traced using equations derived in section 3b with (U, V) being the adjusted estimate of barotropic mesoscale current, $\mathbf{U} = ½\mathbf{U}_{sfc}$. The currents affect the propagation of all modes, although the effect increases with mode numbers.[3]

In addition to modifying the propagation path, mesoscale currents also affect the group and phase speeds. To quantify this effect, weekly realizations of the sea surface velocity field are calculated using Aviso data from September of 2001 to September of 2002. Modes 1–5 are generated in the Kauai Channel and propagated through the mesoscale field toward the Farfield site. Probability density functions for the group arrival time anomalies are given in Fig. 11. To obtain the group arrival time anomalies, the times that particular wave groups take to reach a line parallel to the Hawaiian Ridge going through the Farfield site (i.e., a line oriented at $-30°$ from the east, at 430 km from the ridge) are compared with the time required in the absence of currents. Table 1 lists the group propagation times and their standard deviations for each mode.

Because wave crests travel faster than the group $(c_P > c_G)$, the phase of the internal tide is not constant following a group. In comparing the phase at a given distance from the ridge with and without advection, however, the biggest effect is the difference in group propagation times (i.e., difference in group propagation times is a good proxy for phase differences).

Throughout the year, mode 1 always reaches the Farfield within ± 2 h of the expected time. The delays for mode 2 are roughly a factor of 2 larger (± 4 h). From Fig. 11, modes 3 and higher can be significantly delayed and therefore effectively appear to have random phases. This loss of coherence is investigated in the next section. Note that delays in the arrival of the groups are never more than ~ 4 h for modes 1 and 2.

The expected phase of the internal tide at the HOME Farfield site can be compared with direct observations. Modes 1 and 2 are fitted to the isopycnal displacement time series calculated from the temperature sensors on a mooring of the HOME tomography array (P. Worcester and B. Dushaw 2004, personal communication), deployed about 30 km from the location of *FLIP* between September of 2001 and April of 2002. The measured displacement phases (offset so that the displacements of mode 1 have a zero phase on average) are plotted as the gray lines in Fig. 12. Also plotted (as solid circles) are the phases of isopycnal displacements at the Farfield (offset so that the mean phase of mode 1 is zero) resulting from using the ray equations derived above, generating an internal wave in the Kauai Channel, and propagating it to the Farfield through the mesoscale field calculated from the Aviso sea surface

[3] The spatial structure of the mesoscale field is taken to be frozen in time. This is a good approximation for the very low modes because they propagate over distances that are large in comparison with the eddy scale in a day. The time evolution of the mesoscale should be considered in calculating the refraction of the higher modes.

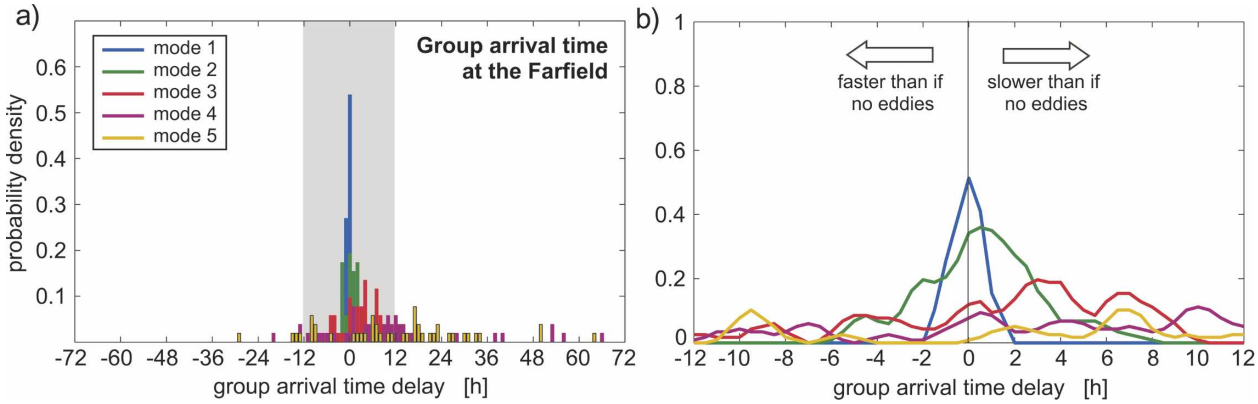

FIG. 11. (a) Probability density functions of group arrival times, showing the delay or advance (h) in arrival times of modes 1–5 propagating from the Kauai Channel to the Farfield through the Aviso mesoscale eddy field ($\mathbf{U} = \frac{1}{2}\mathbf{U}_{sfc}$) relative to the case without mesoscale currents. (b) Same as in (a) but zooming on the ±12 h range (gray shading). Fifty-two weekly velocity fields are used to compute the probability density functions (September 2001–September 2002).

heights for every week from September of 2001 to September of 2002. The model for propagation, despite its marginally valid assumptions, does a fair job in predicting the magnitude of the phase variations and the relative increase of variation between modes 1 and 2. For mode 1, the observed rms phase delay is 0.20π rad, as compared with 0.12π rad for the model. These rms values increase to 0.58π and 0.42π for the observed and predicted phase delays of mode 2.

The simple model described here is appropriate only if generation is uniform along the ridge. The Hawaiian Ridge is not a line source (Rudnick et al. 2003; Lee et al. 2006), however. Given that most of the internal tides observed in the Farfield site probably originate from the Kauai Channel, it might have been more appropriate to vary the "launch angle" of each mode and compare the phases of those waves that eventually pass through the Farfield site as mesoscale conditions vary.

c. *Internal wave propagation along T/P track 112*

With a repeat period of about 10 days, the T/P altimeter would not appear to be an ideal instrument to study tidal signals. Because internal tides are initially forced at precisely the astronomic tidal frequencies, however, the altimeter data can be bandpass filtered around the tidal aliasing frequencies (62.1 days for the M_2 tide) to obtain tidal sea surface elevations (Ray and Mitchum 1996, 1997). The barotropic tidal signal dominates, but the surface manifestation of the internal tide is also detectable, appearing as an oscillation with amplitude of several centimeters and wavelength of 50–150 km. The T/P-inferred phase of the internal tide indicates propagation away from the Hawaiian Ridge while the amplitude decays away from the ridge on a 1000-km scale. This slow decrease in measured sea surface elevation could be due to a true loss of amplitude

TABLE 1. Time required for modes 1–5 to propagate from the Kauai Channel to the Farfield site; T_{G_0} is the group propagation time in the case of no currents, and T_G is the time required when propagating through the mesoscale eddy field ($\mathbf{U} = \frac{1}{2}\mathbf{U}_{sfc}$). The standard deviation for each mode is listed (in hours).

	T_{G_0} (days)	$\langle T_G \rangle$ (days)	$[\langle (T_G - T_{G_0})^2 \rangle]^{1/2}$ (h)
Mode 1	1.72	1.72	0.7
Mode 2	3.18	3.20	2.6
Mode 3	4.88	5.02	7.8
Mode 4	6.51	7.02	20.5
Mode 5	8.01	9.15	63.8

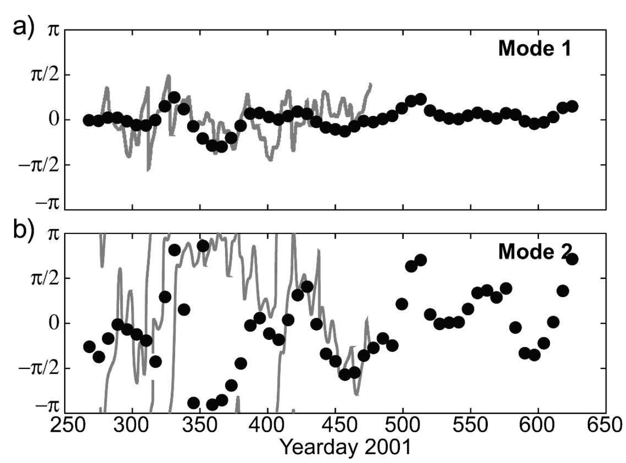

FIG. 12. Time series of the phase of isopycnal displacements for (a) mode 1 and (b) mode 2, comparing direct observations (fits to the displacement inferred from the S3 mooring, solid lines) and as obtained using the ray equations through the observed mesoscale velocity field (section 3b).

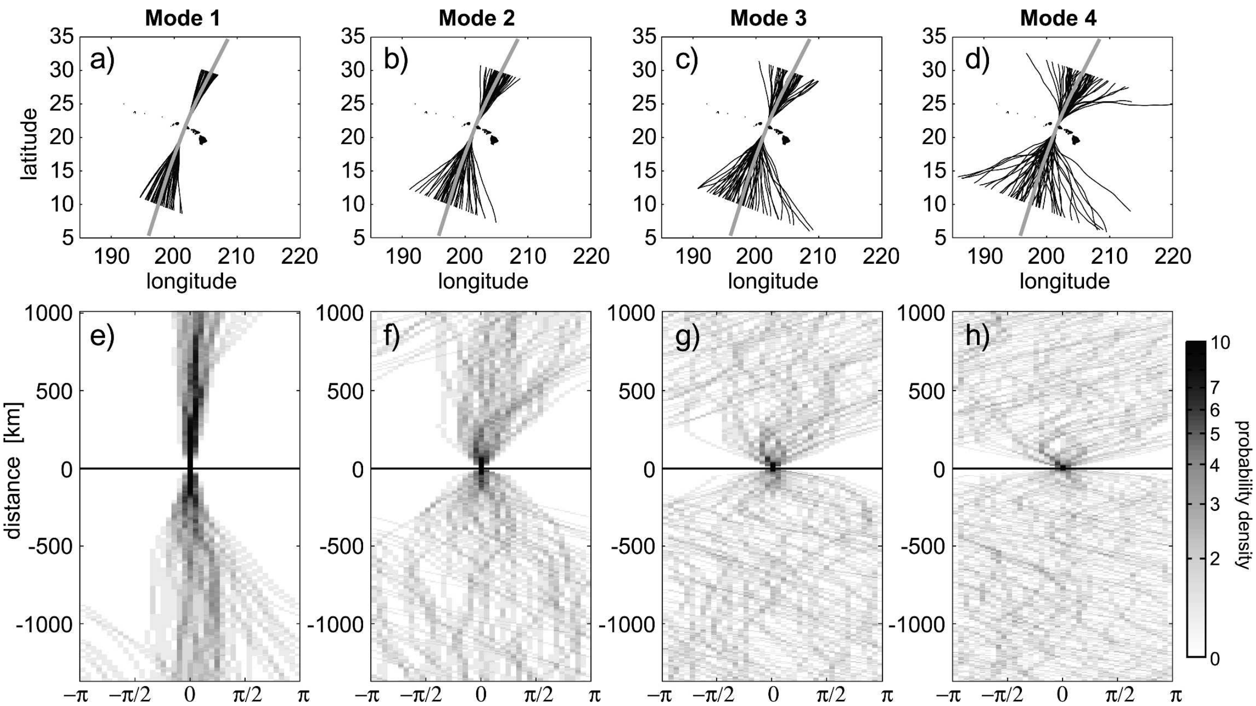

FIG. 13. (a)–(d) Paths of modes 1–4 propagating through the mesoscale eddy field for 52 weeks (September 2001–September 2002). Internal waves are generated in the Kauai Channel and launched along T/P track 112 (gray line). (e)–(h) Phase offsets (relative to no currents) as functions of distance plotted as probability densities.

of the wave through dissipation, the departure of a confined beam of energy from the T/P track, or a loss of temporal coherence with the astronomical forcing. Here, we address whether the observed current variability near Hawaii is sufficient to cause this loss of coherence. Data along T/P track 112, which passes near the HOME Farfield site, are used.

The propagation paths of modes 1–4 for 52 weeks (September 2001–September 2002) are shown in Figs. 13a–d. As before, modes are generated in the Kauai Channel (21.6°N, 158.5°W) and launched along track 112 (i.e., with initial propagation angles of −111° and 69° with respect to east for waves propagating southward and northward, respectively). The spread due to the mesoscale variability increases with mode number.

As in the previous section, the phase of the internal wave modes as they reach a given distance away from the ridge is investigated. Figures 13e–h show probability density functions of the phase (relative to the case of zero current) as functions of distance for modes 1–4. This is calculated from the difference between the phase of the modes as they reach a line parallel to the ridge, labeled by the distance from the ridge to the point at which this line crosses T/P track 112, and the phase it would have in the absence of currents. Phase lags remain relatively small for mode 1, and to a certain extent for mode 2 (within 200 or 300 km), but quickly become random for higher modes. Note that the increase of phase variability with distance is larger south of the Hawaiian Ridge.

When measurements of the sea surface manifestation of the internal tide taken at a fixed distance from the ridge are averaged together with respect to a given phase (e.g., referenced to the barotropic phase, as in the T/P analysis), the signal decreases with distance because of the loss of coherence, even if the amplitude of the internal tide remains constant. To illustrate this effect, Fig. 14 shows the sea surface height manifestation of mode 1 as a function of distance along T/P track 112, assuming a uniform maximum midwater isopycnal displacement of 10 m, consistent with the observations at the HOME Farfield site. The phase of the internal tide is not locked to the barotropic tide, however, and its variability as a function of distance is described in Fig. 13e. Figure 14 was obtained by averaging 52 weekly sea surface height manifestations of mode 1, calculated from propagating mode 1 through the mesoscale eddy field from Aviso sea surface height. The barotropic velocities are taken to be $\mathbf{U} = \mathbf{U}_{sfc}$ (Fig. 14a), $\mathbf{U} = \frac{1}{2}\mathbf{U}_{sfc}$ (Fig. 14b), and $\mathbf{U} = \frac{1}{3}\mathbf{U}_{sfc}$ (Fig. 14c). High-passed sea surface elevations measured by T/P are shown in black (Ray and Mitchum 1996, 1997).

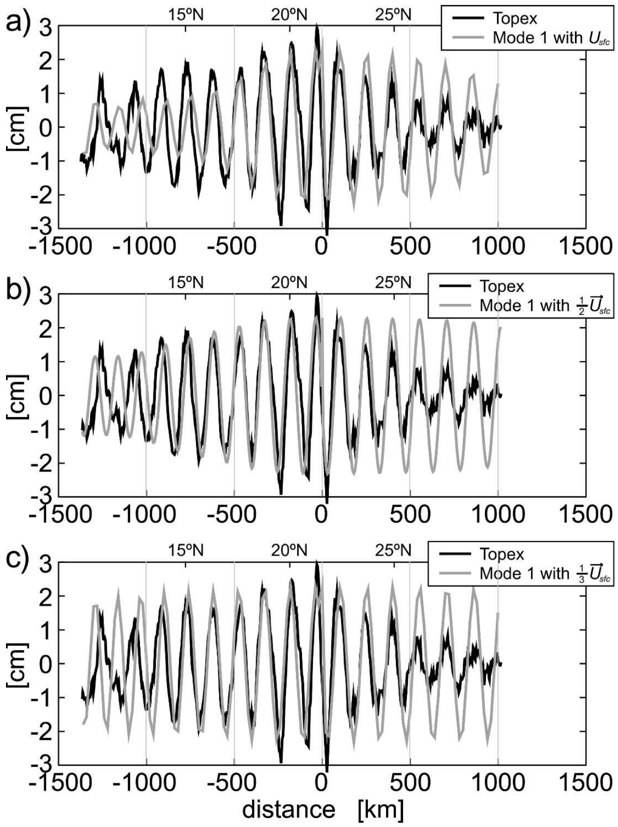

FIG. 14. Sea surface manifestation of the M_2 internal tide for a mode-1 wave propagating from Hawaii (distance = 0) with a constant amplitude but losing coherence because of mesoscale currents (gray; Fig. 13), as compared with the signal measured by T/P along track 112 (black). Depth-integrated currents are set to (a) 1, (b) ½, and (c) ⅓ times the surface currents from Aviso sea surface height. Best agreement south of Hawaii is seen in (b).

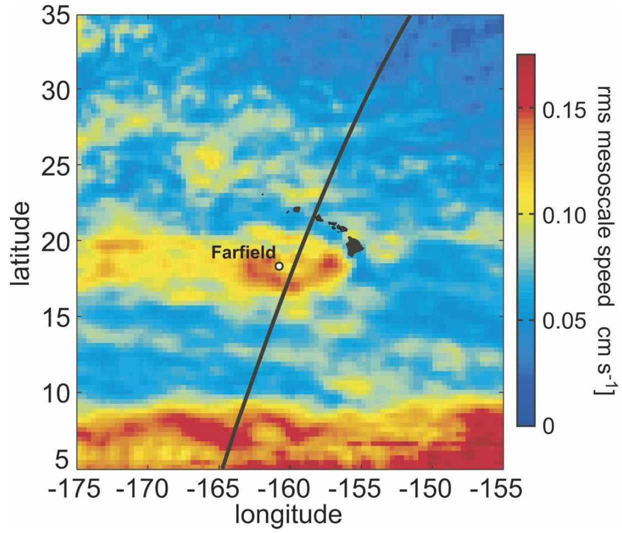

FIG. 15. Map of the rms mesoscale speed ($\mathbf{U}$ = ½$\mathbf{U}_{sfc}$) around Hawaii, computed from 52 weeks (September 2001–September 2002). Large variability is seen southwest of Hawaii.

South of the Hawaiian Ridge (negative distances), the case $\mathbf{U}$ = ½$\mathbf{U}_{sfc}$ (Fig. 14b) shows good agreement between the constant-amplitude model and the observations. Larger barotropic velocities (Fig. 14a) introduce too much phase variability, and smaller velocities (Fig. 14c) lead to too much phase coherence.

For distances greater than 1000 km, the wavelength of the T/P baroclinic tide becomes larger than the modeled mode-1 wavelength. A suggested explanation for this discrepancy is that the internal tide is no longer propagating parallel to track 112 at these ranges.

In contrast to the southward propagation, the observed sea surface manifestation north of the ridge is always smaller than the modeled one, even in the case in which $\mathbf{U} = \mathbf{U}_{sfc}$. The propagation model predicts that the internal tide should remain highly coherent and phase locked to the barotropic tide for very large distances. As seen in the map of rms barotropic mesoscale velocity (with $\mathbf{U}$ = ½$\mathbf{U}_{sfc}$) around Hawaii (Fig. 15), strong eddies are observed just south of the Hawaiian Islands and in the equatorial regions, but there is very little variability on the north side of Hawaii. The northward-propagating internal tide therefore should remain more coherent with the astronomical forcing.

We conclude that the mesoscale variability can degrade the coherence in the T/P observations south of the Hawaiian Ridge sufficiently to explain the apparent amplitude attenuation. There is no need to invoke dissipative processes. On the other hand, internal tides propagating northward should remain coherent over great distances. The apparent decay in the T/P observations requires a physical explanation.

One hypothesis is that the northward beam is less parallel to T/P track 112 than its southern counterpart. However, numerical predictions of conversion at the ridge (Merrifield et al. 2001; Simmons et al. 2004) indicate that waves should propagate nearly along the track, even north of the ridge. Further comparisons are needed.

A second hypothesis is that nonlinear transfers become more effective at extracting energy from the internal tide as it propagates northward. In particular, the generation of subharmonics might be dramatically enhanced near the latitude at which ½M_2 waves are purely inertial (28.9°) (Hibiya and Nagasawa 2004; J. MacKinnon and K. Winters 2005, personal communication). Both numerical and observational investigations of this apparent discrepancy are in progress. Topographic scattering (Johnston and Merrifield 2003) is probably not important along the track considered here.

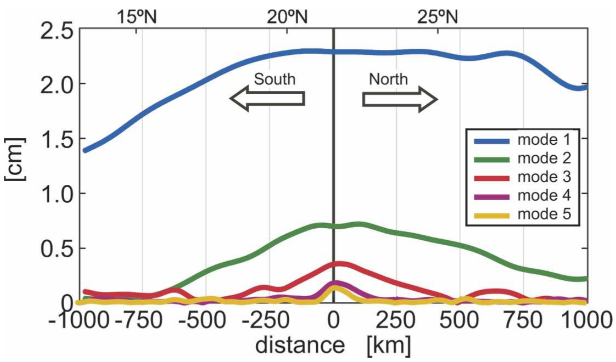

FIG. 16. Predicted amplitude of M_2 sea surface height along T/P track 112 for modes 1–5. All modes have a maximum vertical displacement of 10 m. The distance over which modes are coherent rapidly decreases with mode number. Note the asymmetry between the south and north sides of the Hawaiian Ridge.

Relative to mode 1, higher modes are expected to lose coherence with the astronomical forcing relatively rapidly (Fig. 16). The amplitude of the sea surface manifestation that would be obtained from a long average is plotted versus distance for modes 1–5. Mode 2 can be detected to distances of a few hundred kilometers. Higher modes are very rapidly rendered incoherent by the mesoscale velocity field.

5. Summary

The propagation of the low-mode internal tide in an ocean with realistic topography, stratification, and mesoscale current variability is investigated. A time-invariant climatological ocean is considered first. Wave group speed is significantly reduced over shallow topographic features such as the Mid-Atlantic Ridge and East Pacific Rise. Group speed gradually decreases with increasing latitude, eventually vanishing at the turning latitude. The change of buoyancy frequency at the subtropical front (lat 30°–35°) results in a sharp decrease of both group and phase speeds. Internal wave modes are significantly refracted away from regions of large phase speed.

The initial ray equations are then extended to include refraction by barotropic mesoscale currents. These are applied to interpret data from the HOME Farfield site and to reconcile the in situ observations with sea surface elevations made along nearby T/P line 112. The effect of currents becomes more dramatic as mode number increases. In the Hawaii observations, the path of mode 1 is weakly affected (although its phase becomes increasingly random as the distance from its source increases). The coherence of modes 3 and higher is dramatically reduced by the local mesoscale current.

Based on the work presented here, we speculate that the strong variability of the low-mode internal tide often observed on the continental slope (e.g., off Virginia; Nash et al. 2004), is due in part to the interaction of a remotely generated internal tide with the meandering Gulf Stream. Strong interaction between the Kuroshio and the local near-inertial field has recently been reported (Rainville and Pinkel 2004).

To the southwest of Hawaii, along T/P track 112, phase fluctuations induced by mesoscale eddies are sufficient to explain the observed decay in sea surface height associated with the M_2 internal tide (Ray and Mitchum 1997), as measured by T/P. It is not necessary to invoke energy dissipation to account for the signal decay. On the north side, however, there is very little eddy variability and the internal tide should remain phase coherent. However, the observed sea surface signal decays faster than on the south side. Additional investigation is required to determine whether this asymmetry is due to localized generation and cross-track propagation, direct dissipation, bottom scattering, or more efficient energy transfer by nonlinear interactions.

The WKB approach yields fundamental insight into the global propagation of internal waves. As with all applications of this approximation, however, the underlying simplicity is obtained at the expense of some realism. To be specific, although the large-scale hydrographic features of the planet are adequately treated, the scale separation between the longest internal waves and the ocean mesoscale is not large. Young and Ben Jelloul (1997) note that this problem is particularly severe for near-inertial waves, whose horizontal wavelengths can exceed quasigeostrophic scales. They derive a new governing dynamics to describe this interaction. In the present case, with a focus on the tides ($\lambda_H = 150$ km), the accuracy of the approximation is significantly better.

The added assumption of modal propagation is also an approximation. It will fail in regions of rapid topographic change where scattering ("mode conversion" in acoustics) becomes important. Wave interaction with geostrophic shear is inherently a three-dimensional problem, with small changes in shear or wave speed leading to potentially large changes in outcome. Despite these complexities, we feel that the WKB approach is a tractable and valuable means of exploring basic aspects of global wave propagation.

Acknowledgments. We thank Eric Slater, Mike Goldin, Mai Bui, Jerry Smith, Lloyd Green, and the other members of the Ocean Physics Group at SIO for their help in collecting data during HOME. We acknowledge

Dr. John Colosi, Dr. Matthew Alford, and two anonymous reviewers for the comments and suggestions on this work. We also thank the HOME principal investigators, the National Science Foundation, and the Office of Naval Research.

APPENDIX A

Internal Wave Equation in the Presence of Horizontal Advection

With advection by large-scale depth-independent currents, the equations of motion become (Gill 1982; Kunze 1985)

$$\partial_t u + U\partial_x u + V\partial_y u - fv = -\rho_0^{-1}\partial_x p, \quad \text{(A1)}$$

$$\partial_t v + U\partial_x v + V\partial_y v + fu = -\rho_0^{-1}\partial_y p, \quad \text{(A2)}$$

$$\partial_t w + U\partial_x w + V\partial_y w = -\rho_0^{-1}\partial_z p - g\rho_0^{-1}\rho', \quad \text{(A3)}$$

$$\partial_t \rho' + U\partial_x \rho' + V\partial_y \rho' = \frac{N^2\rho_0}{g}w, \quad \text{and} \quad \text{(A4)}$$

$$\partial_x u + \partial_y v + \partial_z w = 0, \quad \text{(A5)}$$

where $\partial_{x_i} = \partial/\partial_{x_i}$. The interaction terms involving the mean flow shear [terms of the form $(\mathbf{u}\cdot\boldsymbol{\nabla})\mathbf{U}$] are neglected because both the vorticity and the vertical shear of the flow are small ($0.9f < f_{\text{eff}} < 1.1f$). The goal here is to derive an equation of the form of the internal wave equation [Eq. (1); see, e.g., Gill (1982)]. The y derivatives of f and spatial derivatives of the barotropic field (U, V) are ignored ($\partial_{x_i}U \ll \partial_{x_i}u$). Differentiating Eq. (A1) with respect to t and x and Eq. (A2) with respect to t and y, substituting the result into ∂_{tt} [Eq. (A5)], and differentiating with respect to z, one obtains

$$\begin{aligned}-\rho_0^{-1}(\partial_{xx} + \partial_{yy})\partial_{tz}p + f\partial_{tz}(\partial_x v - \partial_y u) + \partial_{tt}\partial_{zz}w \\ - \partial_{tz}(U\partial_x + V\partial_y)(\partial_x u + \partial_y v) = 0. \quad \text{(A6)}\end{aligned}$$

The vorticity equation, obtained by differentiating Eq. (A1) with respect to y and Eq. (A2) with respect to x [and using Eq. (A5)], is equal to

$$\partial_t(\partial_x v - \partial_y u) = f\partial_z w + (U\partial_x + V\partial_y)(-\partial_x v + \partial_y u). \quad \text{(A7)}$$

Using Eq. (A7) and substituting an expression for $-\rho_0^{-1}\partial_{tz}p$ found from Eqs. (A3) and (A4), Eq. (A6) becomes

$$\begin{aligned}&(\partial_{xx} + \partial_{yy})[N^2 w + \partial_{tt}w + (U\partial_x + V\partial_y)(-g\rho_0^{-1}\rho' + \partial_t w)] \\ &\quad + (\partial_{tt} + f^2)\partial_{zz}w + \partial_z[f(U\partial_x + V\partial_y)(-\partial_x v + \partial_y u) \\ &\quad + \partial_t(U\partial_x + V\partial_y)\partial_z w] = 0. \quad \text{(A8)}\end{aligned}$$

Equation (A5) has been used in the last term; ρ' can be expressed in terms of pressure [Eq. (A3)], and, rearranging, we obtain

$$\begin{aligned}&[\partial_{tt}\nabla^2 + f^2\partial_{zz} + N^2(\partial_{xx} + \partial_{yy})]w + [2(U\partial_x + V\partial_y)\partial_t \\ &\quad + (U\partial_x + V\partial_y)^2](\partial_{xx} + \partial_{yy})w \\ &\quad + (U\partial_x + V\partial_y)\partial_z[\partial_x(\rho_0^{-1}\partial_x p - fv) \\ &\quad + \partial_y(\rho_0^{-1}\partial_y p + fu) + \partial_{tz}w] = 0. \quad \text{(A9)}\end{aligned}$$

The first bracket is the traditional internal-wave equation. Using Eqs. (A1) and (A2), and rearranging,

$$\begin{aligned}&[(\partial_{tt} + f^2)\partial_{zz} + N^2(\partial_{xx} + \partial_{yy})]w + [2(U\partial_x + V\partial_y)\partial_t \\ &\quad + (U\partial_x + V\partial_y)^2](\partial_{xx} + \partial_{yy} + \partial_{zz})w = 0. \quad \text{(A10)}\end{aligned}$$

This is equal to Eq. (21).

APPENDIX B

Derivation of the Hamiltonian Function in the Presence of Currents

Although the structure of the vertical modes for low-frequency internal waves does not change in the presence of barotropic mesoscale currents, the advective terms in the eigenvalue must be retained:

$$\left\{\frac{(\partial_{xx} + \partial_{yy})[\tilde{w} \quad \exp(-i\omega t)]}{[(\partial_t + \mathbf{U}\cdot\boldsymbol{\nabla})^2 + f^2][\tilde{w} \quad \exp(-i\omega t)]}\right\} \equiv \frac{1}{c_e^2}. \quad \text{(B1)}$$

This can be written as

$$\begin{aligned}&[(c_e^2 - U^2)\partial_{xx} + (c_e^2 - V^2)\partial_{yy} + \omega^2 - f^2 - 2UV\partial_{xy} \\ &\quad + 2i\omega U\partial_x + 2i\omega V\partial_y]\tilde{w} = 0. \quad \text{(B2)}\end{aligned}$$

Equation (B2) is the Helmholtz equation for modes propagating through a nonuniform and moving medium.

We assume that $\tilde{w}$ is composed of a slowly varying amplitude multiplying a wave form [Eq. (7)]. Substituting in Eq. (B2) and retaining only the real (physical) part, we obtain

$$\begin{aligned}&(c_e^2 - U^2)[\partial_{xx}A - \omega^2 A(\partial_x\phi)^2] - 2\omega^2 AU\partial_x\phi + (c_e^2 - V^2) \\ &\quad \times [\partial_{yy}A - \omega^2 A(\partial_y\phi)^2] - 2\omega^2 AV\partial_y\phi \\ &\quad - 2UV(\partial_{xy}A - \omega^2 A\partial_x\phi\partial_y\phi) - Af^2 + A\omega^2 = 0. \quad \text{(B3)}\end{aligned}$$

Because A is a slowly varying function of x and y, the terms of order ω^2 dominate, and Eq. (B3) becomes

$$\begin{aligned}&(c_e^2 - U^2)(\partial_x\phi)^2 + (c_e^2 - V^2)(\partial_y\phi)^2 + 2U\partial_x\phi + 2V\partial_y\phi \\ &\quad - 2UV\partial_x\phi\partial_y\phi - 1 + \frac{f^2}{\omega^2} = 0. \quad \text{(B4)}\end{aligned}$$

By defining $\nabla\phi = (p_x, p_y)$, the Hamiltonian function used in section 3b is defined from Eq. (B4) as

$$H \equiv (c_e^2 - U^2)p_x^2 + (c_e^2 - V^2)p_y^2 + 2Up_x + 2Vp_y - 2UVp_xp_y - 1 + \frac{f^2}{\omega^2} = 0. \quad \text{(B5)}$$

REFERENCES

Alford, M., 2001: Internal swell generation: The spatial distribution of energy flux from the wind to mixed later near-inertial motions. *J. Phys. Oceanogr.,* **31,** 2359–2368.

——, 2003: Redistribution of energy available for ocean mixing by long-range propagation of internal waves. *Nature,* **423,** 159–163.

Boyer, T., C. Stephens, J. Antonov, M. Conkright, R. Locarnini, T. O'Brien, and H. Garcia, 2002: *Salinity*. Vol. 2, *World Ocean Atlas 2001,* NOAA Atlas NESDIS 50, 165 pp.

Chiswell, S., 2002: Energy levels, phase, and amplitude modulation of the baroclinic tide off Hawaii. *J. Phys. Oceanogr.,* **32,** 2640–2651.

Colosi, J., 2006: Geometric sound propagation through an inhomogeneous and moving ocean: Scattering by small scale internal wave currents. *J. Acoust. Soc. Amer.,* **119,** 705–708.

Ducet, N., P. L. Traon, and G. Reverdin, 2000: Global high-resolution mapping of ocean circulation from TOPEX/Poseidon and *ERS-1* and *-2*. *J. Geophys. Res.,* **105,** 19 477–19 498.

Dushaw, B., B. Cornuelle, P. Worcester, B. Howe, and D. Luther, 1995: Barotropic and baroclinic tides in the central North Pacific Ocean determined from long-range reciprocal acoustic transmissions. *J. Phys. Oceanogr.,* **25,** 631–647.

Egbert, G., and R. Ray, 2000: Significant dissipation of tidal energy in the deep ocean inferred from satellite altimeter data. *Nature,* **405,** 775–778.

Ferrari, R., and D. Rudnick, 2000: Thermohaline variability in the upper ocean. *J. Geophys. Res.,* **105,** 16 857–16 883.

Gill, A., 1982: *Atmosphere–Ocean Dynamics.* Academic Press, 662 pp.

Hibiya, T., and M. Nagasawa, 2004: Latitudinal dependence of diapycnal diffusivity in the thermocline estimated using a finescale parameterization. *Geophys. Res. Lett.,* **31,** L01301, doi:10.1029/2003GL017998.

Jensen, F., W. Kuperman, M. Porter, and H. Schmidt, 2000: *Computational Ocean Acoustics.* Springer, 580 pp.

Johnston, T., and M. Merrifield, 2003: Internal tide scattering at seamounts, ridges, and islands. *J. Geophys. Res.,* **108,** 3180, doi:10.1029/2002JC001528.

Jones, R., 2001: The dispersion relation for internal acoustic-gravity waves in a baroclinic fluid. *Phys. Fluids,* **13,** 1274–1280.

Kantha, L., and C. Tierney, 1997: Global baroclinic tides. *Progress in Oceanography,* Vol. 40, Pergamon, 163–178.

Kunze, E., 1985: Near-inertial wave propagation in geostrophic shear. *J. Phys. Oceanogr.,* **15,** 544–565.

——, and T. Sanford, 1984: Observations of near-inertial waves in a front. *J. Phys. Oceanogr.,* **14,** 566–581.

Lee, C., E. Kunze, T. Sanford, J. Nash, M. Merrifield, and P. Holloway, 2006: Internal tides and turbulence along the 3000-m isobath of the Hawaiian Ridge. *J. Phys. Oceanogr.,* **36,** 1165–1183.

Lighthill, J., 2002: *Waves in Fluids.* 2d ed. Cambridge University Press, 520 pp.

Lozovatsky, I., E. Morozov, and H. Fernando, 2003: Spatial decay of energy density of tidal internal waves. *J. Geophys. Res.,* **108,** 3201, doi:10.1029/2001JC001169.

MacKinnon, J. A., and K. B. Winters, 2005: Subtropical catastrophe: Significant loss of low-mode tidal energy at 28.9°. *Geophys. Res. Lett.,* **32,** L15605, doi:10.1029/2005GL023376.

Merrifield, M., P. Holloway, and T. Johnston, 2001: The generation of internal tides at the Hawaiian Ridge. *Geophys. Res. Lett.,* **28,** 559–562.

Miropol'sky, Y., 2001: *Dynamics of Internal Gravity Waves in the Ocean.* Kluwer Academic, 406 pp.

Müller, P., 1976: On the diffusion of momentum and mass by internal gravity waves. *J. Fluid Mech.,* **77,** 789–823.

——, and N. Xu, 1992: Scattering of oceanic internal gravity waves off random bottom topography. *J. Phys. Oceanogr.,* **22,** 474–488.

Munk, W., 1981: Internal waves and small scale processes. *Evolution of Physical Oceanography,* B. Warren and C. Wunsch, Eds., The MIT Press, 264–291.

Nash, J., E. Kunze, J. Toole, and R. Schmitt, 2004: Internal tide reflection and turbulent mixing on the continental slope. *J. Phys. Oceanogr.,* **34,** 1117–1133.

Niwa, Y., and T. Hibiya, 2001: Numerical study of the spatial distribution of the M_2 internal tide in the Pacific Ocean. *J. Geophys. Res.,* **106,** 22 441–22 449.

Olbers, D., 1981: Propagation of internal waves in a geostrophic current. *J. Phys. Oceanogr.,* **11,** 1224–1233.

Peters, H., 1983: The kinematics of a stochastic field of internal waves modified by a mean shear current. *Deep-Sea Res.,* **30,** 119–148.

Phillips, O., 1977: *The Dynamics of the Upper Ocean.* 2d ed. Cambridge University Press, 336 pp.

Rainville, L., and R. Pinkel, 2004: Observations of energetic high-wavenumber internal waves in the Kuroshio. *J. Phys. Oceanogr.,* **34,** 1495–1505.

——, and ——, 2006: Baroclinic energy flux at the Hawaiian Ridge: Observations from the R/P *FLIP*. *J. Phys. Oceanogr.,* **36,** 1104–1122.

Ray, R., and G. Mitchum, 1996: Surface manifestation of internal tides generated near Hawaii. *Geophys. Res. Lett.,* **23,** 2101–2104.

——, and ——, 1997: Surface manifestation of internal tides in the deep ocean: Observations from altimetry and island gauges. *Progress in Oceanography,* Vol. 40, Pergamon, 135–162.

Rudnick, D., and Coauthors, 2003: From tides to mixing along the Hawaiian Ridge. *Science,* **301,** 355–357.

Simmons, H., R. Hallberg, and B. Arbic, 2004: Internal wave generation in a global baroclinic tide model. *Deep-Sea Res. II,* **51,** 3043–3068.

Stephens, C., J. Antonov, T. Boyer, M. Conkright, R. Locarnini, T. O'Brien, and H. Garcia, 2002: *Temperature*. Vol. 1, *World Ocean Atlas 2001,* NOAA Atlas NESDIS 50, 167 pp.

St. Laurent, L., and C. Garrett, 2002: The role of internal tides in mixing the deep ocean. *J. Phys. Oceanogr.,* **32,** 2882–2899.

Thorpe, S., 1978: On internal gravity waves in an accelerating flow. *J. Fluid Mech.,* **88,** 623–639.

Wunsch, C., 1997: The vertical partition of oceanic horizontal kinetic energy. *J. Phys. Oceanogr.,* **27,** 1770–1794.

Young, W., and M. Ben Jelloul, 1997: Propagation of near-inertial oscillations through a geostrophic flow. *J. Mar. Res.,* **55,** 735–766.